JOURNAL OF PETROLOGY | VOLUME 52 | NUMBER 4 | PAGES 717–731 | 2011 | doi:10.1093/petrology/egq101

Experimental Evidence for a Reduced Metal-saturated Upper Mantle

ARNO ROHRBACH[1,2,3]*, CHRIS BALLHAUS[3], PETER ULMER[1], UTE GOLLA-SCHINDLER[2] AND DIRK SCHÖNBOHM[3]

[1]INSTITUT FÜR GEOCHEMIE UND PETROLOGIE, ETH ZÜRICH, SONNEGGSTRASSE 5, 8092 ZÜRICH, SWITZERLAND
[2]INSTITUT FÜR MINERALOGIE, UNIVERSITÄT MÜNSTER, CORRENSSTR. 24, 48149 MÜNSTER, GERMANY
[3]STEINMANN INSTITUT FÜR GEOLOGIE, MINERALOGIE, PALÄONTOLOGIE, UNIVERSITÄT BONN, POPPELSDORFER SCHLOSS, 53115 BONN, GERMANY

RECEIVED JANUARY 15, 2010; ACCEPTED DECEMBER 30, 2010
ADVANCE ACCESS PUBLICATION JANUARY 28, 2011

The uppermost mantle as sampled by xenoliths, peridotite massifs and primitive basaltic melts appears to be relatively oxidized, with oxygen fugacities between the magnetite–wüstite and fayalite–ferrosilite–magnetite equilibria. Whether this range in oxygen fugacity is a shallow mantle signature or representative of the entire upper mantle still is unclear and a matter of debate because mantle regions deeper than 200 km are not well sampled. To constrain the redox state of the deeper upper mantle, we performed experiments from 1 to 14 GPa and 1220 to 1650°C on a model peridotite composition, encompassing the convecting asthenospheric mantle down to the Transition Zone at 410 km depth. The experiments were run in iron metal capsules to buffer fO_2 *close to an oxygen fugacity about 0·5 log units below the iron–wüstite equilibrium. Analysis of the experimental phases for ferric iron using electron energy loss spectroscopy reveals that at pressures higher than 7 GPa, subcalcic pyroxene and majoritic garnet incorporate appreciable amounts of ferric iron, even though at the experimental conditions they were in redox equilibrium with metallic iron. The major ferric iron carrier in the upper mantle is majoritic garnet, followed by subcalcic pyroxene. At around 8 ± 1 GPa, corresponding to ~250 ± 30 km depth in the upper mantle, sufficient quantities of subcalcic pyroxene and majoritic garnet are stabilized that all the ferric iron thought to be present in fertile upper mantle (i.e. ~2000 ppm) can be accommodated in solid solution in these phases, even though they were synthesized in redox equilibrium with metallic Fe. Based on the results of the experiments, it can be stated that, on a global scale, an oxidized upper mantle near the fayalite–ferrosilite–magnetite equilibrium is the exception rather than the rule. More than 75 vol. % of the Earth's present-day mantle is likely to be saturated with metallic iron.*

KEY WORDS: *mantle; redox; experimental petrology; majorite; EELS; disproportionation; ferric iron*

INTRODUCTION

The oxidation state, next to pressure and temperature, is one of the most fundamental intensive parameters of the Earth's mantle. The oxidation state of the mantle, quantified as the fugacity of oxygen or fO_2, determines in a volatile-bearing mantle which C–H–O volatiles are the stable species. Oxygen fugacity also determines, through volatile speciation, the pressure–temperature position of the mantle solidus. Mantle material in equilibrium with oxidized H_2O–CO_2 volatiles and/or carbonate phases has a lower solidus temperature than mantle in equilibrium with reduced CH_4 and H_2. Oxygen fugacity also affects the rheological properties of the mantle. An H_2O-bearing (oxidized) mantle with high concentrations of hydroxyl in nominally anhydrous silicates is less viscous in a convective regime than a dry (reduced) mantle (Kohlstedt *et al.*, 1996). It is not surprising that considerable effort has gone into quantifying oxidation states and understanding the parameters that control fO_2 in the mantle.

The uppermost mantle appears to be moderately oxidized. Spinel- and plagioclase-bearing peridotites from orogenic massifs, abyssal peridotites and mantle xenoliths in basalts span a range in fO_2 relative to the fayalite–magnetite–quartz (FMQ) equilibrium from 3·4 log units below to about 1·5 log units above FMQ; that is, FMQ − 3·4 to FMQ + 1·5 (Ballhaus *et al.*, 1990, 1991; Ballhaus,

*Corresponding author. Telephone +41 44 63 27803. Fax +41 44 63 21636. E-mail: arno.rohrbach@erdw.ethz.ch

1993; Frost & Ballhaus, 1998, Foley, 2010, and references therein). Garnet-bearing peridotites appear, on average, to be slightly more reduced. Equilibria involving ferric and ferrous iron in pyroxene and garnet give relative fO_2 values ranging from FMQ − 4·2 to around FMQ (see Frost & McCammon, 2008). The most reduced values have been recorded from deep-seated garnet harzburgite and lherzolite xenoliths from Archaean cratonic lithosphere (Woodland & Koch, 2003; McCammon & Kopylova, 2004) where the highest pressure xenoliths tend to return the lowest relative fO_2.

Partial melts of the upper mantle, in comparison, are systematically more oxidized than mantle peridotite samples. Mid-ocean ridge basalts (MORB) range from FMQ − 1·5 to ~FMQ (Christie *et al.*, 1986; Bezos & Humler, 2005), ocean island basalts (OIB) from FMQ to around FMQ + 1·5 (Ballhaus, 1993), and convergent margin basalts up to FMQ + 3, in rare instances (Luhr & Carmichael, 1981, 1985) up to as high as FMQ + 5. The reason for this difference probably lies in the partial melting process generating basalts. Ferric iron components in minerals are more incompatible during partial melting than ferrous iron components (e.g. Arculus, 1994), so the partial melt always has a higher ferric to total iron ratio ($Fe^{3+}/\Sigma Fe$) than the mantle source from which it was generated, leading to relative oxidation when the melt is segregated and rises to the surface (Ballhaus & Frost, 1994). The residue left after melt segregation should in turn be more reduced than the melt; however, usually refractory mantle tends to be more oxidized than fertile mantle. This is so because melt segregation not only removes ferric and ferrous iron oxides, but also lowers the buffering capacity of the residue with respect to fO_2 by depleting it in iron, leaving a depleted harzburgite much more susceptible to later oxidation events than a fertile mantle.

In contrast to the upper mantle, the Transition Zone and the lower mantle appear to be highly reduced, with relative fO_2 up to two log units below the iron–wüstite equilibrium (IW − 2). Because no natural samples exist from these mantle regions from which to calculate fO_2, relative fO_2 estimates need to be based on theoretical considerations (Ballhaus, 1995) and experiments (O'Neill *et al.*, 1993*b*; Frost *et al.*, 2004; Rohrbach *et al.*, 2007). Pressure stabilizes phases in mantle compositions that can incorporate more ferric iron than minerals stable at low pressure (see Gudmundsson & Wood, 1995; Woodland & O'Neill, 1995). Therefore, assuming that the Fe_2O_3 content of the bulk mantle remains constant with depth, increasing pressure leads to a decrease in the activities of the ferric iron components in the various mantle phases, because a given amount of ferric iron can be distributed among an increasing mineral reservoir fractionating ferric iron. This causes the relative fO_2 to fall. Most notable is the early observation by Bell & Mao (1975) that FeO may disproportionate with increasing pressure to Fe_2O_3 and metallic Fe in a basaltic system. This observation was later confirmed and quantified by Frost *et al.* (2004) to hold for mantle compositions as well. Once Fe metal becomes a stable phase, the mantle is well buffered with respect to fO_2.

In this study we establish a redox profile through the convecting upper mantle. We report the results of experiments on a model mantle composition in redox equilibrium with metallic Fe from 1 to 14 GPa and 1220 to 1650°C, to quantify how much ferric iron can be incorporated in pyroxene and garnet at a given pressure, when the relative fO_2 is buffered by equilibrium with Fe metal. Pyroxenes and garnet in the run products were analyzed for their $Fe^{3+}/\Sigma Fe$ ratios with electron energy loss spectroscopy (EELS). Between 7 and 9 GPa pressure, sub-calcic pyroxene and majoritic garnet become so abundant, and their ability to fractionate ferric iron so marked, that all the ferric iron present in a fertile mantle composition (i.e. ~2000 ppm Fe_2O_3; O'Neill *et al.*, 1993*a*) can be accommodated in these phases, even though they are in redox equilibrium with metallic Fe. Hence, at depths greater than ~250 km, the chemical potentials of the ferric iron components in the phases and relative fO_2 are sufficiently low that Fe metal may be a stable accessory phase.

EXPERIMENTAL AND ANALYTICAL METHODS

The starting composition of the experiments was a primitive mantle composition originally defined by Palme & O'Neill (2003). To increase the amount of potentially Fe^{3+}-bearing phases (i.e. pyroxene and garnet) the model mantle was depleted by 30% in its normative olivine content. The bulk composition was also enriched in FeO compared with natural mantle (McDonough & Sun, 1995; Palme & O'Neill, 2003), to a molar MgO/(MgO + FeO) ratio of 0·5, to raise the FeO content of the phases and facilitate ferric iron analysis by electron energy loss spectroscopy (EELS). Following these manipulations, the composition of the starting material was 47·5 wt % SiO_2, 0·29 wt % TiO_2, 6·45 wt % Al_2O_3, 0·56 wt % Cr_2O_3, 26·2 wt % FeO, 14·7 wt % MgO, 3·8 wt % CaO, and 0·5 wt % Na_2O.

The initial starting material was prepared from the oxides SiO_2, TiO_2, Cr_2O_3, Al_2O_3, and MgO, and the carbonates $CaCO_3$ and Na_2CO_3. The mix was finely ground in acetone and decarbonated by stepwise heating to 900°C. Ferrous iron oxide was added as commercially available $Fe_{1-x}O$ oxide after the decarbonation step, to avoid oxidation to ferric iron. After addition of the $Fe_{1-x}O$, the mixture was pressed to pellets and sintered for 6 h at 1150°C in a reducing $CO–CO_2$ (222:78) gas atmosphere whose oxygen partial pressure was near the iron–wüstite equilibrium (Deines *et al.*, 1976). This step ensured

that prior to the experiments, the ferric iron content in the starting material was negligible.

Following the sintering step, the pellets were crushed, re-ground to a powder, and aliquots of the powder were pressed into Fe metal capsules. The Fe capsules, after they were filled with silicate but still open, were repeatedly evacuated and flushed with argon to eliminate any possible oxygen from air trapped inside the oxide powder, then sealed under an argon atmosphere by pressing on a conical iron metal lid.

Experimental conditions

Runs from 1 to 3 GPa were performed in an end-loaded piston-cylinder press at the University of Münster, from 1220 to 1400°C. The sample capsules were contained in talc–Pyrex–MgO sleeves, and the heating elements were graphite tubes. Run temperatures were measured with WRe_3–WRe_{25} (type D) thermocouples and controlled to within ±5°C. Runs were quenched at ~250°C s^{-1} by switching off the power supply.

Experiments from 6 to 14 GPa were performed with the 600 and 1000 t Walker-type multi-anvil presses at the High Pressure Laboratory of the Institute for Geochemistry and Petrology at ETH Zurich. Run temperatures in these presses ranged from 1400 to 1650°C and were limited by the thermal stability of the metallic Fe capsule. Pressure was transmitted with 32 mm tungsten carbide (WC) anvils, and the heating elements were stepped $LaCrO_3$ furnaces. Experiments from 6 to 10 GPa used 18/11 assemblies (i.e. 18 mm edge-length of the MgO/Cr_2O_3 ceramic octahedra, 11 mm truncation of WC cubes), and the runs at 12 and 14 GPa used 14/8 assemblies. Temperatures were measured with $PtRh_6$–$PtRh_{30}$ (type B) thermocouples. Both pressure and temperature were computer-controlled, and runs were quenched at a rate of ~1000°C s^{-1} by turning off the power supply. Table 1 summarizes the run times and run conditions of both the piston-cylinder and multi-anvil experiments.

Sample preparation and major element analysis

Experimental charges were mounted in epoxy, polished down to the capsule center, and then documented with backscattered electron (BSE) imaging. The major element compositions of all phases were analyzed using Jeol JXA 8600 and JXA 8900 electron microprobes at the University of Münster, operated at 15 kV accelerating voltage and 15 nA current. Standards used were natural silicates and oxides. Counting times were 20 s on the peak and 5 s on each background. Subsequently, the mounts were polished from the back to obtain a doubly polished thin section 20 μm in thickness. The sections were then glued with acetone-resistant epoxy onto a 75 mesh copper transmission electron microscopy (TEM) grid and detached from the glass slide with acetone. Subsequently, all samples were thinned with a Gatan Duo-mill ion thinning system at 5 kV and 14° beam angle to electron transparency, followed by a 30 min 'cleaning step' at 2·5 kV and 12° beam angle. This cleaning step was applied to remove any amorphous surface material that could have formed during thinning.

Table 1: Experimental conditions and run products

Run number	Experiment type	*P* (GPa)	*T* (°C)	Run duration (h)	Run products
exp10	pc	1	1220	48	ol, opx, cpx
exp15	pc	3	1400	24	px, grt
zuII-4	ma	6	1400	4·5	px, grt
zuIII-1	ma	7	1450	6·0	px, grt/mj
zu8	ma	8	1650	1·5	px, grt/mj, mlt
zuII-3	ma	10	1500	3·5	px, grt/mj
zuIV-1	ma	12	1500	10	px, grt/mj
zuIII-4	ma	14	1500	4·5	grt/mj, mlt

Phases are olivine (ol), clinopyroxene (cpx), orthopyroxene (opx), subcalcic pyroxene (px), garnet (grt), majoritic garnet (mj), and silicate melt (mlt); pc, piston cylinder; ma, multi-anvil.

Electron energy loss spectroscopy (EELS)

The EELS measurements were performed with a Zeiss Libra 200 field emission transmission electron microscope at the University of Münster, operated at 200 kV. Energy filtering was achieved with an in-column omega filter. The energy resolution of the Zeiss Libra is 0·9 eV, measured as full width at half maximum (fwhm) of the zero loss peak. Prior to the EELS measurements, the mineral phases were identified with a Noran EDX system attached to the TEM system. We analyzed 5–14 grains of each mineral phase per run product to obtain a reasonable average. Natural magnetite was measured and quantified routinely as a secondary standard. The EEL spectra were recorded in the order (1) zero loss peak, (2) Fe $L_{2,3}$ edge (three times at 10 s, 30 s and 60 s counting time), and (3) zero loss peak. Background intensity at the $L_{2,3}$ edges was subtracted both in the form of an inverse power-law function and as a double arc-tan function, as described by van Aken *et al.* (1998). No oxidation of the samples, formation of amorphous layers, or beam-induced contamination was observed during the measurements. Deconvolution of the spectra to eliminate multiple scattering processes was found to be unnecessary. The energy scale was calibrated to 707·8 eV for the maximum of the L_3 Fe^{2+} peak and 720·7 eV for the maximum of the L_2 Fe^{2+} peak (van Aken *et al.*, 1998). The spectra were quantified with respect to $Fe^{3+}/\Sigma Fe$ ratio using the 'universal curve' method of van

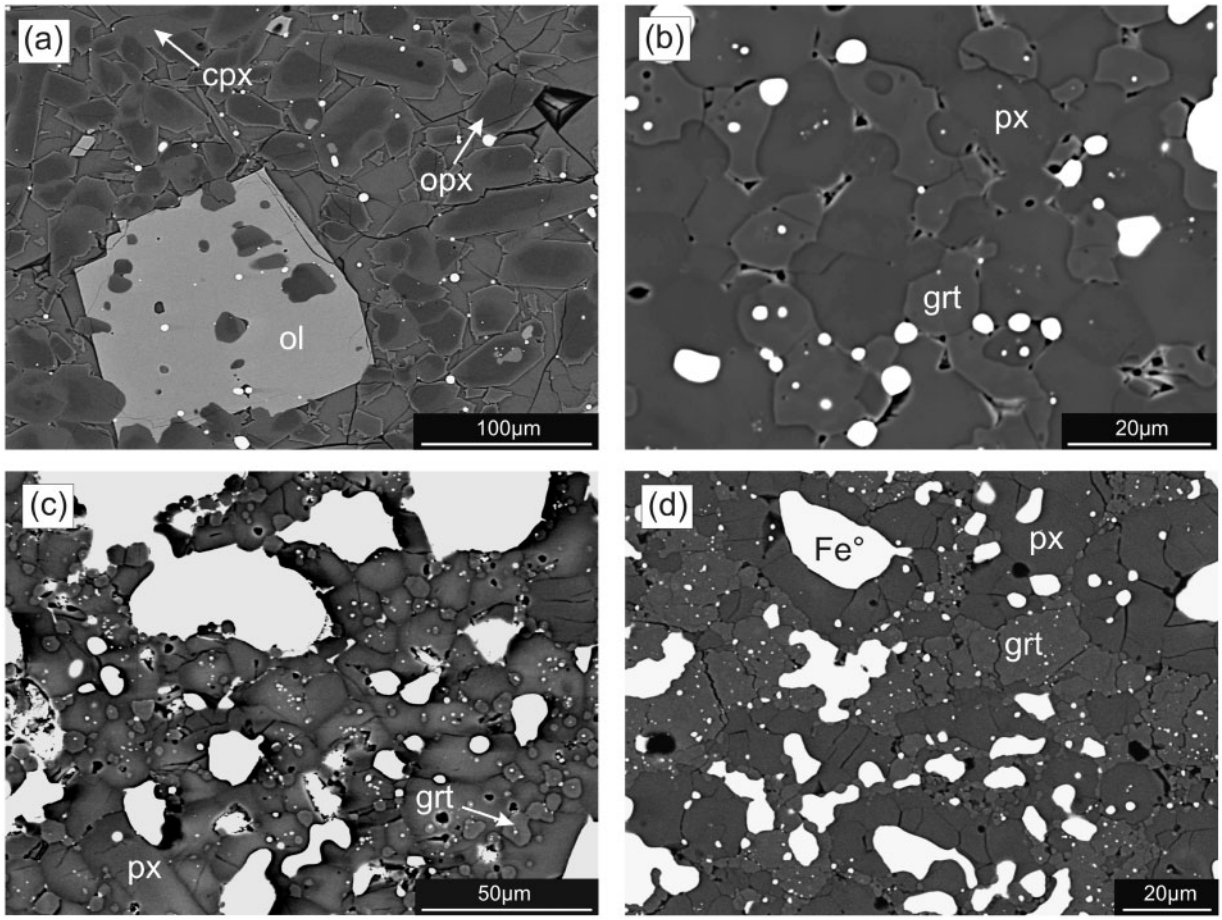

Fig. 1. BSE images of experimental charges. (a) 1 GPa run; phases present are olivine, clinopyroxene and orthopyroxene. Both pyroxenes are zoned towards an equilibrium pigeonitic composition. (b) 3 GPa run; phases from 3 to 12 GPa are subcalcic pyroxene of pigeonitic composition and garnet. (c, d) 10 and 12 GPa runs; all silicate grains are in intimate contact with metallic Fe, suggesting that redox equilibrium was reached.

Aken *et al.* (1998) with improved curve parameters published by van Aken & Liebscher (2002). That calibration uses two integration windows of 2 eV widths each, applied to the Fe L_3 edge from 708·5 to 710·5 eV and to the L_2 edge from 719·7 to 721·7 eV. The ratio of integrated L_3–L_2 peak intensities of these windows allows direct quantification of the $Fe^{3+}/\Sigma Fe$ ratio. The universal curve is based on a range of natural minerals and synthetic solid solutions with varying $Fe^{3+}/\Sigma Fe$ ratios (i.e. hercynite–magnetite, almandine–skiagite, and skiagite–andradite solid solutions) for which the ferric iron concentration was characterized by micro-Mössbauer spectroscopy and electron microprobe analysis (see also Lauterbach *et al.*, 2000; Frost & Langenhorst, 2002; Frost *et al.*, 2004).

RUN PRODUCTS

Figure 1 shows BSE images of typical run products. The 1 GPa run (1220°C) crystallized olivine and two pyroxenes. In the 3–6 GPa runs, stable silicate phases were subcalcic pyroxene plus an almandine-rich garnet, whereas olivine was not identified, because it either was too rare or was absent. This is because we depleted the starting material in normative olivine and enriched it in FeO. The 7–12 GPa runs also crystallized subcalcic pyroxene and garnet (no olivine found), but in this pressure range garnet becomes increasingly majoritic in composition. In the highest pressure (14 GPa) run, the only silicate phase identified was a distinctly majoritic garnet.

In addition to these phases, all experimental charges were peppered with micrometer-sized grains of metallic iron, both along grain boundaries and as inclusions within silicates. Some of the iron grains may be due to disproportionation of ferrous iron at run conditions, whereas others may constitute material mobilized from the sample capsule and re-precipitated inside the charge. Regardless, the distribution of metal grains provides good textural evidence that redox equilibrium between silicate and Fe

metal was generally achieved. Judging from the ubiquity of cavities along grain boundaries and at triple junctions, we suspect that most charges experienced very slight degrees of partial melting (Fig. 1b), although melt was never preserved as glass. Mass-balance calculations do favor an additional phase present at run conditions, but because melt is not preserved, we were unable to determine its composition. Because all the conclusions reached from our experiments are based on exchange and redox equilibria among crystalline phases, minor loss of a melt phase is immaterial for the argument presented and the conclusions reached.

Mineral compositions

Figure 2 shows the molar $Mg/(Mg+Fe^{2+})$ ratios, henceforth Mg-number, of pyroxene and garnet as a function of run pressure. Generally, the Mg-number of the phases is close to the bulk Mg-number of the starting composition, which was 0·5. Exceptions are the 8 and 14 GPa run products where the phases are distinctly more magnesian than the phases in the other runs. Our preferred explanation is that both runs experienced some degree of partial melting. Because melt was not accounted for it might have been lost from the charges by capsule leakage, depleting the phases in FeO. All other experiments follow a trend of a slight increase in Mg-number with increasing pressure. We attribute this trend to the precipitation of Fe metal owing to disproportionation of FeO at pressures greater than 6 GPa (see below), to ferric iron and metallic Fe, depleting the silicates in FeO. Average phase compositions are shown in Electronic Appendices 1 and 2 (available at http://www.petrology.oxfordjournals.org).

Olivine was present only in the 1 GPa experiment (Fig. 1a) and constituted an estimated 15 vol. % of the charge. Compositions range around Fo_{40}; that is, they are slightly more iron-rich than the Mg-number of the starting composition, possibly caused by limited oxidation of Fe from the sample capsule to FeO, possibly by trapped air.

Pyroxene is the most abundant phase in all runs to up to 7 GPa, constituting 60–70 vol. %. Above this pressure, modal pyroxene decreases steadily in favor of garnet because pyroxene components substitute into the garnet structure to form a majorite solid solution as pressure increases. Usually, pyroxene was found to be homogeneous in its major element composition, with slight variations around $En_{47}Fs_{43}Wo_{10}$ (Fig. 3). Exceptions are the 1 and 8 GPa runs. In the 1 GPa experiment, two pyroxene generations were found, a Ca-poor pyroxene with 2 mol % wollastonite component, and a subcalcic clinopyroxene generation with 15 mol % Wo (Fig. 1a). It should be noted that although that both pyroxenes were found to be zoned towards a common composition of $En_{47}Fs_{43}Wo_{10}$, it is possible that crystallization of olivine locally generated low Mg/Si micro-environments, initially stabilizing a low-Ca

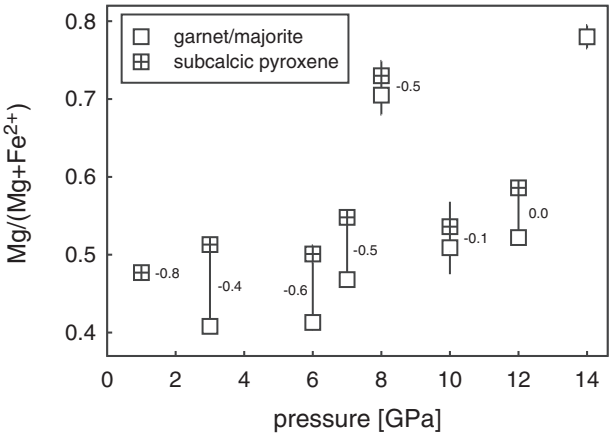

Fig. 2. $Mg/(Mg+Fe^{2+})$ vs pressure of subcalcic pyroxene and garnet/majorite$_{ss}$. Molar Mg-number calculated after subtraction of ferric iron (EELS data) from total Fe analyzed as FeO by EPMA. Numbers next to the symbols are $\Delta\log f O_2$ [IW] values deduced from the molar fractions of FeO in pyroxene. Uncertainties are standard errors of the mean at the 95% confidence level.

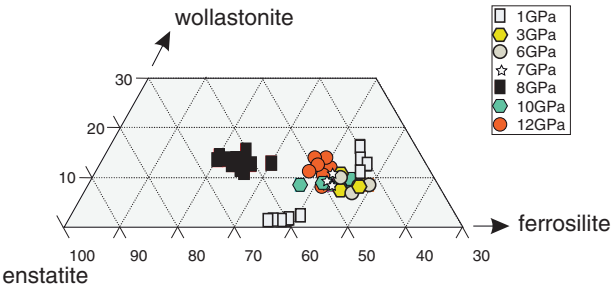

Fig. 3. Pyroxene compositions plotted in terms of wollastonite–enstatite–ferrosilite as a function of pressure. At 1 GPa two pyroxenes are present, and at 8 GPa pyroxene is enriched in the enstatite component owing to minor loss of FeO-rich melt (see text).

pyroxene that equilibrated towards a more CaO-rich composition as run time progressed. As noted above in relation to Mg-number, the 8 GPa run might have contained higher proportions of an FeO-enriched melt owing to the higher run temperature, rendering residual phases more magnesian than the bulk composition. Average pyroxene compositions are reported in Electronic Appendix 1.

Garnet is the second most abundant phase in the experiments at pressures ≥3 GPa and increases in modal abundance with increasing pressure. In the highest-pressure run (14 GPa), majoritic garnet is the only crystalline silicate. Garnet grains are 5–20 μm in size and largely euhedral (Fig. 1), sometimes poikiloblastic in shape overgrowing pyroxene. Atomic Mg-number is usually lower than that of the coexisting pyroxenes, and close to the Mg-number of the starting composition. An exception is

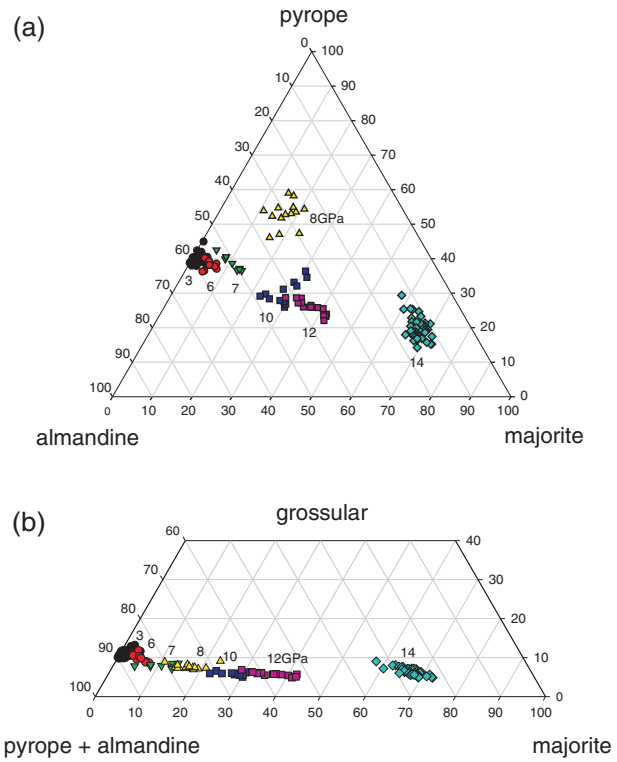

Fig. 4. Garnet compositions. (a) Pyrope–almandine–majorite components, majorite increasing with pressure. The 8 GPa garnets are enriched in the pyrope component. (b) (Pyrope + almandine)–grossular–majorite components; gradual increase in majorite component with decreasing grossular content.

the 8 GPa run where garnets are as magnesian as the coexisting pyroxenes. Garnet compositions are shown in Fig. 4 and electron probe microanalysis (EPMA) averages reported in Electronic Appendix 2.

Oxygen fugacities at run conditions

Oxygen fugacities (fO_2) during the experimental runs were calculated from the ferrosilite activity in subcalcic pyroxene, assuming that redox equilibrium with the Fe was attained. Textural evidence (i.e. the presence of tiny Fe metal grains dispersed throughout all the silicate phases) supports this. The relevant ferrosilite–quartz/coesite–iron (fs–qtz–iron) equilibrium is

$$2Fe^0 + O_2 + 2SiO_2 = Fe_2Si_2O_6. \quad (1)$$

Oxygen fugacities are expressed relative to this equilibrium, as

$$\Delta \log fO_2[\text{fs} - \text{qtz} - \text{iron}] = \log a_{\text{Fs}}^{\text{px}} - 2\log a_{\text{Fe}}^{\text{metal}} - 2\log a_{SiO2}. \quad (2)$$

At the high run temperatures employed here, it is justified to assume that cations mix ideally on the M1 and M2 sites of pyroxene (O'Neill & Wall, 1987) where

$$\log a_{\text{Fs}}^{\text{px}} = \log \left(X_{\text{Fe}}^{\text{M1}} X_{\text{Fe}}^{\text{M2}}\right). \quad (3)$$

The calculations used molar FeO contents in pyroxene calculated after subtraction of $FeO_{1\cdot5}$ as determined by EELS (see below). There is an apparent problem to be addressed in that silica activity (a_{SiO2}) appears unconstrained by the experimental mineral assemblages. Apart from the 1 GPa run, no olivine was found, and neither was a crystalline SiO_2 phase (e.g. β-quartz or coesite) stable. Because relative fO_2 as calculated from equation (2) is a_{SiO2} dependent, any uncertainty in log a_{SiO2} feeds into relative fO_2 by a factor of two.

Tschermaks molecule concentrations in the pyroxenes, themselves a_{SiO2} dependent because Al on the tetrahedral site competes with Si, suggest that silica activities were closer to olivine than to SiO_2 phase saturation. This is because the experimental pyroxenes synthesized here are similar in Tschermaks concentrations to natural, low-calcium pyroxenes in olivine-bearing mantle rocks (see Luth & Canil, 1993). To the relative fO_2 values thus calculated were added the respective contributions from a_{SiO2}, as if all pyroxenes coexisted with olivine of similar Mg-number. Minimum silica activity at run pressure and temperature was calculated from the equilibrium

$$Mg_2SiO_4 + SiO_2 = Mg_2Si_2O_6 \quad (4)$$

using the mixing model of O'Neill & Wall (1987) and Perple_X programs (Connolly, 1990; Connolly & Petrini, 2002), which apply the thermodynamic database of Holland & Powell (1998).

We relate $\Delta \log fO_2$ [fs–qtz–iron] values to the IW equilibrium by calculating the fO_2 difference between the two equilibria at run pressures and temperatures (Electronic Appendix 1). We use the expression of O'Neill (1987) for IW and Perple_X programs to calculate the fs–qtz–iron equilibrium. The values relative to IW thus calculated are noted next to the symbols in Fig. 2, illustrating that relative fO_2 variations among the runs are small up to 8 GPa. Oxygen fugacity conditions in the 10 and 12 GPa experiments are close to IW and appear to be slightly less reducing owing to low a_{SiO2} calculated at the highest pressures. It should be noted that these fO_2 values are maximum values as no olivine was observed at pressures higher than 1 GPa.

Pyroxene–garnet element partitioning

Below 6 GPa, garnet has a near-perfect $M_3Al_2Si_3O_{12}$ stoichiometry; however, above that pressure it becomes distinctly majoritic in composition (Fig. 4), with Si p.f.u. >3.

Majorite substitution reflects the elevated solubility of the pyroxene component in the garnet structure with increasing pressure, according to

$$2\,M_2Si_2O_6(cpx) + M_3Al_2Si_3O_{12}(grt) = M_3Al_2Si_3O1_2 \times xM_3(MSi)Si_3O_{12}(maj_{ss}) \quad (5)$$

where M = Mg and Fe^{2+}. As majorite in garnet increases (Fig. 4a and b) the grossular component decreases. Evidently, in peridotitic bulk compositions CaO avoids the majoritic garnet component and concentrates in pyroxene, so long as pyroxene is stable.

Our dataset (bulk Mg-number = 0·5) is compared in Fig. 5 with previous experiments on mantle peridotite compositions (higher bulk Mg-number of 0·9; Irifune, 1987; Akaogi & Akimoto, 1979; Herzberg & Zhang, 1996). The proportion of the majorite component in garnet is expressed as $Si_{(3+x)}$ excess over stoichiometric garnet (Si = 3) and shown as a function of run pressure. Also shown is the respective decrease in Al + Cr cations. Included in Fig. 5 are data from experiments in the peridotite + 5 wt % CO_2 system with a bulk Mg-number = 0·9 (A. Rohrbach & M. W. Schmidt, unpublished data), where the pressure–temperature conditions were close to an adiabat in the asthenospheric upper mantle. Figure 5 shows that for any given pressure, there is a considerable range in majorite content in garnet. This range is largely due to temperature; at a given pressure the lowest majorite content corresponds to the lowest run temperature (Akaogi & Akimoto, 1979; Irifune, 1987) and the highest concentration to the highest temperature experiment (Herzberg & Zhang, 1996). Regardless of temperature and bulk composition, the onset of measurable majorite in garnet appears to be the same in all datasets (i.e. around 5–6 GPa). The pressure at which pyroxene is completely dissolved in garnet (13·5–15·8 GPa; Fig. 5) is also identical within ~2 GPa. We conclude, therefore, that even though our mantle composition was depleted in olivine and enriched in FeO, it still reproduces the phase relations in a natural (more magnesian) mantle reasonably well.

Equally pressure-sensitive is the distribution of Na and Ca between garnet and pyroxene. The exchange observed can be described by the coefficient

$$K\mathrm{D}^{\mathrm{grt-px}}_{\mathrm{Na-Ca}} = x_1(1 - x_2)/[(1 - x_1)x_2] \quad (6)$$

where x_1 = Na + Ca in garnet and x_2 = Na + Ca in pyroxene (Sobolev & Lavrent'ev, 1971). Up to about 6 GPa, $K\mathrm{D}^{\mathrm{grt-px}}_{\mathrm{Na-Ca}}$ is pressure independent (Fig. 6). Above 6 GPa, however, we notice a sharp increase in $K\mathrm{D}^{\mathrm{grt-px}}_{\mathrm{Na-Ca}}$ controlled by the exchange vector $Si^{VI}NaAl^{VI}_{-1}Ca_{-1}$. This coupled substitution can operate only if Si (and maybe Ti) is present in garnet on the octahedral site. Therefore, Na in garnet increases with increasing pressure.

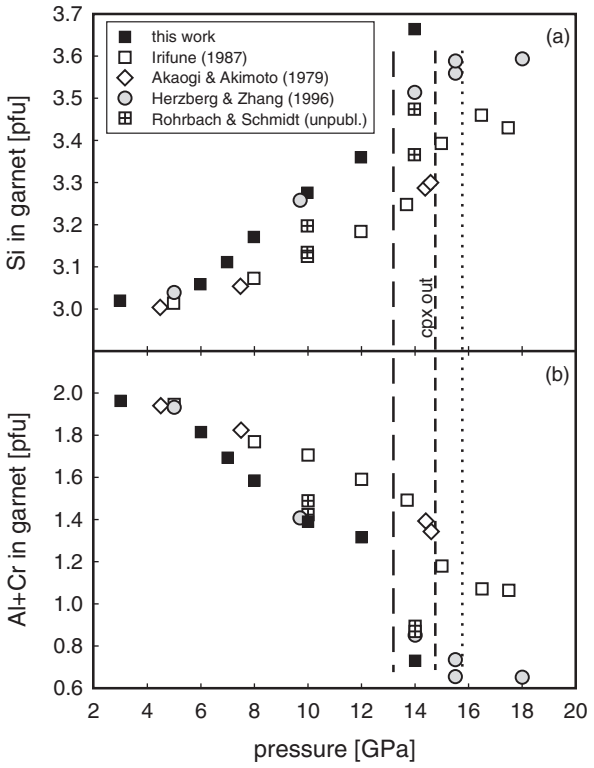

Fig. 5. Si and (Al + Cr) cations in the garnet/majorite$_{ss}$ vs pressure. Excess Si over stoichiometric garnet reflects the majorite component in garnet. Si increases with increasing pressure, whereas Al and Cr cations show a corresponding decrease. Garnets from close to solidus runs are enriched in the majorite component (Herzberg & Zhang, 1996, and our data) relative to garnets from lower temperature experiments (Akaogi & Akimoto, 1979; Irifune, 1987). Lines marking the pressure at which clinopyroxene is dissolved in garnet are from Herzberg & Zhang (1996; short dashes), Irifune (1987; dotted line) and experiments reported here (long dashes), and are temperature controlled. The unpublished data of A. Rohrbach & M. W. Schmidt are from experiments in a peridotite + CO_2 system at 1400 and 1520°C at 10 GPa, and 1450 and 1620°C at 14 GPa.

Ferric–ferrous iron ratios in pyroxene and garnet

Representative background-corrected EEL spectra of pyroxene and garnet are shown in Fig. 7. Values for experimental pressure and calculated $Fe^{3+}/\Sigma Fe$ ratios are shown next to the spectra. The intensity of the Fe^{3+} peak at 709·5 eV (arrow in Fig. 7b) is directly correlated with the atomic $Fe^{3+}/\Sigma Fe$ ratio. For comparison, we also measured garnets in the 14 GPa run with a sub-ångstrom transmission electron microscope (SATEM) located at Carl Zeiss NTS GmbH, Oberkochen, Germany. The SATEM has an energy resolution of 0·4 eV, which is more than double that of the Zeiss Libra in Münster. As the SATEM is not equipped with an EDX system, and hence is unable to distinguish pyroxene from garnet, only the 14 GPa (garnet-only) run was analyzed with both instruments. The ferrous and ferric iron fractions of the Fe L_3 peak

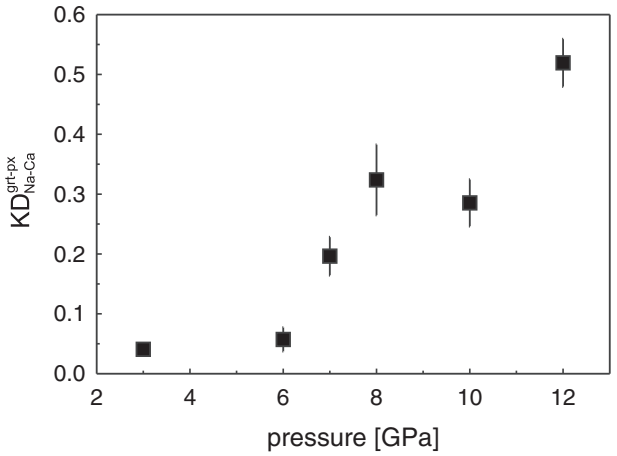

Fig. 6. $K\mathrm{D}^{\mathrm{grt-px}}_{\mathrm{Na-Ca}}$ vs pressure. Sodium is partitioned distinctly into pyroxene at pressures <6 GPa. Above 6 GPa Na partitions progressively into garnet and KD increases. This is because Na incorporation in the garnet structure requires Si in garnet present on the octahedral site.

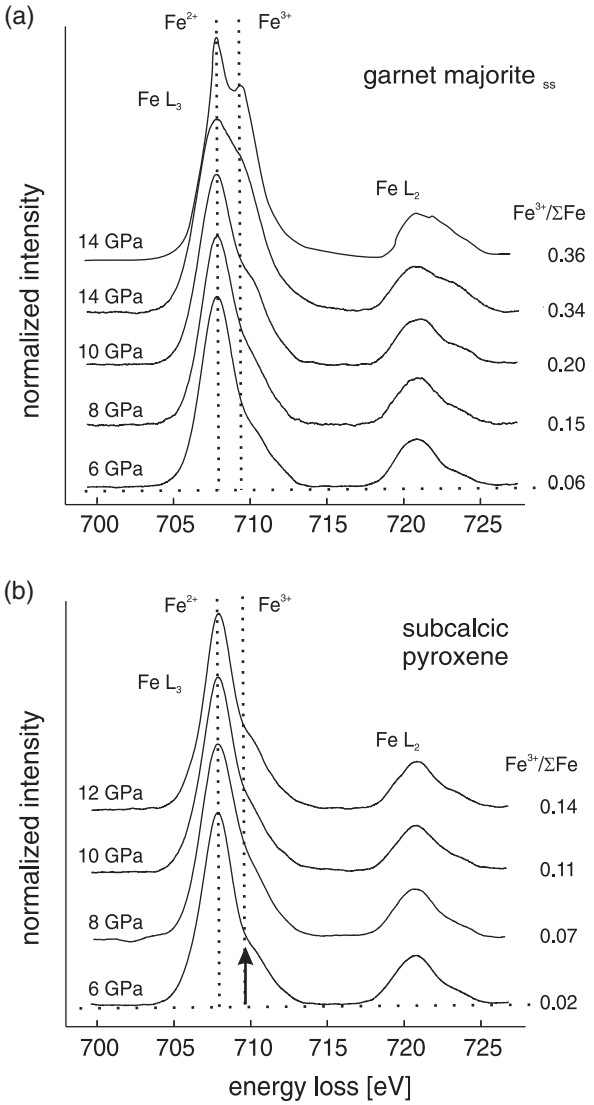

Fig. 7. Representative background subtracted EEL spectra of garnet/majorite$_{ss}$ and subcalcic pyroxene. The increase in the Fe^{3+} peak (L_3 edge) with pressure corresponds to an increase in $Fe^{3+}/\Sigma Fe$ [arrow in (b)]. Spectra measured with Zeiss Libra in Münster, energy resolution is 0·9 eV measured as full width at half maximum of the zero loss peak. Top spectrum in (a) was measured with the SATEM of Carl Zeiss NTS GmbH at Oberkochen; the enhanced energy resolution of 0·4 eV of the SATEM results in an improved resolution of the Fe^{2+}–Fe^{3+} peaks of the L_3 edge. The $Fe^{3+}/\Sigma Fe$ ratios agree with those obtained with the Libra in Münster.

form clearly separated peaks, reflecting the enhanced energy resolution of this spectrum (Fig. 7a, uppermost spectrum). Within the given uncertainty limits for majoritic garnet of the 14 GPa run, the $Fe^{3+}/\Sigma Fe$ ratio obtained with two very different instruments is near-identical, confirming that our measured $Fe^{3+}/\Sigma Fe$ ratios are reproducible.

The change in atomic $Fe^{3+}/\Sigma Fe$ ratio of pyroxene and garnet with experimental pressure is summarized in Fig. 8. Each data point represents the average of 5–14 analyzed grains per charge. Each grain was measured three times, at 10, 30, and 60 s counting time. All spectra were quantified with respect to $Fe^{3+}/\Sigma Fe$ ratio individually to ensure that the specimen was not contaminated nor oxidized during lengthy exposure to the electron beam, as observed by Lauterbach *et al.* (2000). We encountered no oxidation under the beam, even when counting times were increased to 5 min.

Experimental run products at pressures ≤6 GPa are considered essentially ferric iron free. Above 6 GPa, it is possible to resolve an increase in $Fe^{3+}/\Sigma Fe$ ratio with increasing pressure for both subcalcic clinopyroxene and majoritic garnet. Additionally, we notice that garnet is always enriched in ferric iron relative to coexisting clinopyroxene (Fig. 9). This fractionation potentially reflects the positive temperature dependence of the Fe^{3+} exchange between garnet and pyroxene, as noted by Canil & O'Neill (1996) in natural garnet peridotites.

The data available for metal-saturated garnet or majorite for comparison are those of O'Neill *et al.* (1993*b*), McCammon & Ross (2003), and Frost *et al.* (2008). These data provide no evidence for systematic variations in $Fe^{3+}/\Sigma Fe$ with Mg-number, in contrast to $(Mg,Fe)SiO_3$ perovskite (see Frost *et al.*, 2008, fig. 4a and b), so our results may be directly applicable to the natural mantle. The $Fe^{3+}/\Sigma Fe$ ratio in pyroxene at metal saturated conditions seems to be related to the $Fe^{3+}/\Sigma Fe$ of coexisting garnet, as argued above, although experimental data for direct comparison are not available.

To lend additional credence to the accuracy of the $Fe^{3+}/\Sigma Fe$ ratios measured, we show in Fig. 10 the Fe–Mg

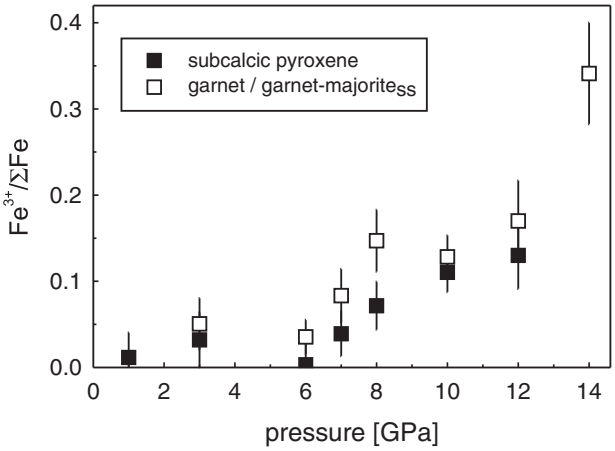

Fig. 8. The $Fe^{3+}/\Sigma Fe$ atomic ratios of pyroxene and garnet/majorite$_{ss}$ vs pressure. Averages of 5–14 analyses per symbol. Error bars are standard errors of the mean with 95% confidence interval, and include variations between analyses and uncertainties in the universal curve parameters of van Aken & Liebscher (2002).

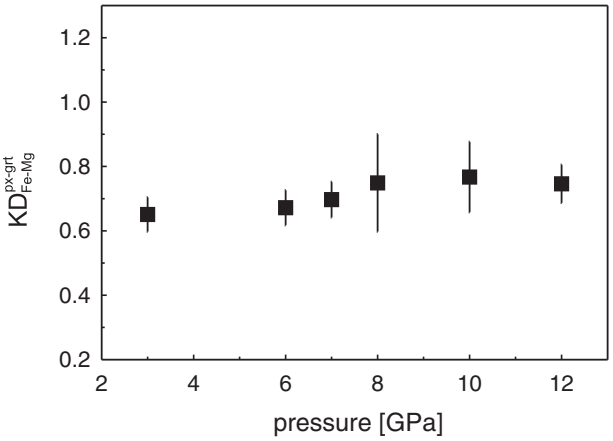

Fig. 10. KD^{px-grt}_{Fe-Mg} vs pressure. The KD varies within error (95% confidence) around 0·7 and is indicative of the attainment of Fe–Mg exchange equilibrium between pyroxene and garnet during the experiments. It should be noted that the KD was calculated with ferrous iron after subtraction of ferric iron as determined by EELS.

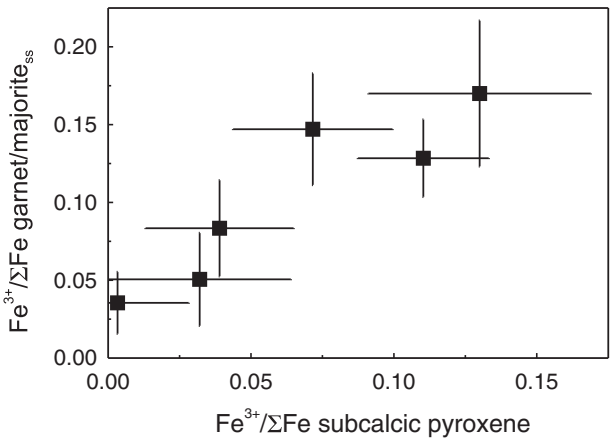

Fig. 9. Ferric iron in garnet vs ferric iron in pyroxene. Correlation between $Fe^{3+}/\Sigma Fe$ ratio in garnet and subcalcic pyroxene. Ferric iron contents in garnet and pyroxene are coupled such that garnet is always the more ferric iron rich phase. Error bars represent standard errors of the mean at a 95% confidence level.

exchange coefficients between pyroxene and garnet, defined as

$$K\mathrm{D}^{\mathrm{px-grt}}_{\mathrm{Fe-Mg}} = X^{\mathrm{px}}_{\mathrm{Fe}} X^{\mathrm{grt}}_{\mathrm{Mg}} / \left(X^{\mathrm{grt}}_{\mathrm{Fe}} X^{\mathrm{px}}_{\mathrm{Mg}} \right). \quad (7)$$

The $K\mathrm{D}_{\mathrm{Fe-Mg}}$ values shown in Fig. 10 were calculated with ferrous iron after subtracting the proportion of ferric iron as determined by EELS from total iron as determined by EPMA. The KD values are uniform around 0·7 in all charges regardless of the Mg-number of each of the phases (see Fig. 2). This result is excellent support for our implicit assumption that equilibrium with respect to Fe–Mg exchange and Fe^{2+}–Fe^{3+} redox equilibria was reached. Interestingly, this also applies to the mineral pairs from the 8 GPa run, which we suspected had lost some FeO–Fe_2O_3-enriched melt. The fact that the KD values are independent of pressure, even though the $Fe^{3+}/\Sigma Fe$ ratios increases markedly with pressure (Fig. 10), supports our implicit assumption that the $Fe^{3+}/\Sigma Fe$ ratios measured are precise and accurate. If there were any systematic errors in ferric iron analysis by EELS, it would be unlikely for the KD^{px-grt}_{Fe-Mg} to remain pressure independent when the Mg-numbers of each of the phases do show considerable inter-experiment variation (see Fig. 2) and do vary with $Fe^{3+}/\Sigma Fe$ and pressure.

DISCUSSION

Our experiments confirm that high-pressure clinopyroxene and garnet can incorporate appreciable amounts of ferric iron, even though the minerals were grown and equilibrated in redox equilibrium with metallic Fe. The starting composition was ferric iron free. Therefore, any $Fe^{3+}/\Sigma Fe$ ratio above zero detected in the product phases must be the result of redox equilibration at run conditions. The measured $Fe^{3+}/\Sigma Fe$ ratios (Fig. 8) are likely to be accurate because they are indirectly confirmed by a remarkable constancy in KD^{px-grt}_{Fe-Mg} (Fig. 10).

Below we explore how much majoritic garnet and subcalcic pyroxene needs to be stabilized to accommodate all the ferric iron in these phases and to drive a fertile mantle composition into Fe metal stability. We discuss the possible equilibria responsible for the generation of ferric iron even in the presence of metallic Fe. We then suggest that the zonation with respect to relative fO_2 within the upper mantle—moderately oxidized at shallow depths and

metal-saturated below ~250 km—can be reconciled within the context of mantle convection.

Depth of metal saturation in the upper mantle

If mineral phases can incorporate ferric iron even though they were synthesized in redox equilibrium with metallic iron, then the converse must be true: fertile upper mantle will reach Fe metal saturation whenever ferric iron-fractionating phases are present in modal quantities sufficient to incorporate all the bulk ferric iron. The bulk ferric iron content in fertile mantle is assumed to be 2000 ppm, as proposed by O'Neill *et al.* (1993*a*). In our experiments and in fertile upper mantle, the important ferric iron carriers are subcalcic clinopyroxene and majoritic garnet (Fig. 8). Both phases are stabilized as pressure and temperature increase with depth. Therefore, the expectation is that relative fO_2 will also fall when pressure and temperature increase along a mantle adiabat.

We may approximate with a simple mass-balance calculation (parameters summarized in Table 2) the depth interval in the upper mantle within which Fe metal saturation is likely to occur. Information required includes the weight proportions and average FeO contents of the mantle phases, as well as the relation between $Fe^{3+}/\Sigma Fe$ and majorite content in garnet, shown in Fig. 11. It should be noted that phase proportions in the mantle vary considerably as a function of pressure. For the calculation here, we have selected the phase proportions relevant for 8–10 GPa. A fertile mantle composition in the garnet stability field at 8–10 GPa crystallizes at about 57 wt % olivine, 20 wt % pyroxene and 23 wt % garnet (Irifune, 1987; Irifune & Isshiki, 1998). For a bulk mantle Mg-number of 0·9, olivine has about 9·8 wt % FeO (i.e. San Carlos olivine composition), subcalcic pyroxene ~4 wt % FeO, and garnet ~7·5 wt % FeO. The latter two concentrations are averaged from mineral analyses reported by Luth *et al.* (1990), Luth & Canil (1993), Canil & O'Neill (1996), and Woodland & Koch (2003). To incorporate the 2000 ppm bulk mantle Fe_2O_3, garnet (23 wt %) must have an $Fe^{3+}/\Sigma Fe$ ratio of 0·080, and pyroxene (20 wt %) an $Fe^{3+}/\Sigma Fe$ ratio of 0·054 (pyroxene $Fe^{3+}/\Sigma Fe$ was calculated using Fig. 9). These ratios correspond to a total of 1510 and 490 ppm Fe_2O_3 stored in garnet and pyroxene, respectively. Consultation of Fig. 11 shows that for a $Fe^{3+}/\Sigma Fe$ ratio of 0·080, garnet requires about 11% of the majorite component. If we apply our data and the near-solidus garnet compositions of Herzberg & Zhang (1996), garnet contains 11% majorite component at ~7 GPa (Fig. 5); if we take the lower-temperature garnet compositions synthesized by Akaogi & Akimoto (1979) and Irifune (1987) as a reference, garnet contains 11% majorite component at ~9·5 GPa.

Based on this mass balance, a fertile mantle composition may reach Fe metal saturation at realistic mantle temperatures at a pressure of around 8 ± 1 GPa. This pressure corresponds to a mantle depth of ~250 ± 30 km. At this pressure, subcalcic pyroxene and majoritic garnet can incorporate all the bulk ferric iron present in fertile upper mantle, even when Fe metal is a stable phase. The result is conditional upon the assumption that the convecting asthenospheric upper mantle indeed contains 8·1 wt % total Fe as FeO, of which 2000 ppm is Fe_2O_3, plus the assumption that these concentrations do not vary in any systematic manner with depth.

Table 2: Ferric and ferrous iron content of mantle phases

	Garnet	Pyroxene	Olivine	Whole-rock*
Phase proportion† (wt %)	22·5	20·7	56·8	
FeO^t (wt %)	7·5	4·0	9·7	8·1
Fe_2O_3 (ppm)	1508	492	0	2000
$Fe^{3+}/\Sigma Fe$‡	0·080	0·054	0	

FeO^t, all Fe as FeO.
*Whole-rock FeO and Fe_2O_3 after O'Neill *et al.* (1993*a*).
†Calculated using vol. % data from Irifune & Isshiki (1998) and phase densities from Irifune (1987).
‡Ratios required to match whole-rock Fe_2O_3 = 2000 ppm.

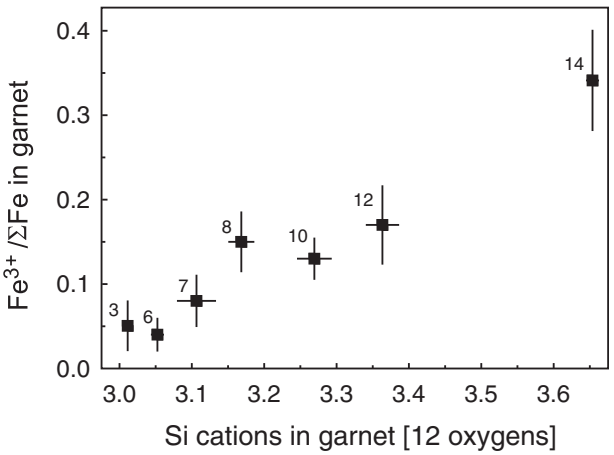

Fig. 11. Correlation between the $Fe^{3+}/\Sigma Fe$ ratio and the Si_{3+x} excess in garnet/majorite$_{ss}$. Values next to the symbols are run pressures in GPa. Error bars are standard errors of the mean with a 95% confidence interval, and include variations between analyses and uncertainties in the universal curve parameters of van Aken & Liebscher (2002).

Source of ferric iron?

In a closed-system situation (i.e. no oxygen added or removed) ferric iron can be generated only by the disproportionation of ferrous iron, according to

$$3FeO = Fe^0 + 2FeO_{1.5}. \quad (8)$$

In relation to mantle petrology and the redox state of the mantle, this idea is not new. Mao (1974) and Mao & Bell (1977) postulated, based on a thermodynamic analysis of the Fe–O system, that FeO should disproportionate to ferric iron and metallic iron at high pressure. Experimental work by Bell & Mao (1975) and Bell *et al.* (1976) supported this idea. Those workers observed that when a basaltic glass was compressed to 15 GPa and heated to 2000°C, the run products (i.e. quench garnet + melt) coexisted with an Fe metal phase even though the initial starting mixes were more oxidized than the IW buffer. The same observation was made by Frost *et al.* (2004). Those workers compressed mantle bulk compositions to lower mantle pressures and also observed metal Fe in the products. Furthermore, Frost *et al.* (2004) could quantify their silicate phases for ferric iron with EELS and Mössbauer spectroscopy, and they demonstrated that silicate perovskite contained appreciable ferric iron even though it was grown in equilibrium with metallic iron.

Experiments and thermodynamic evaluations in the simple Fe–O system are ambiguous with respect to FeO disproportionation. Early thermodynamic data (Mao, 1974; Saxena *et al.*, 1993; Fabrichnaya & Sundmann, 1997) implied that the assemblage magnetite plus metallic Fe could be the high-pressure phase assemblage, indirectly supporting the notion of disproportionation. More recent evaluations of the structure and the thermodynamic properties of $Fe_{1-x}O$ at high pressure (Fei & Mao, 1994; Fei *et al.*, 1999; Haavik *et al.*, 2000; Struzhkin *et al.*, 2001; Lazor *et al.*, 2004), however, have questioned this, and now consensus is emerging that in the Fe–O system, slightly metal-deficient wüstite is the high-pressure phase, not the assemblage magnetite plus metallic Fe. If this result was applicable directly to natural mantle compositions (more complex than Fe–O) there would be no FeO disproportionation.

This poses a problem, for in our experiments there is no source for ferric iron other than from FeO disproportionation. The addition of oxygen during run conditions is unlikely to cause oxidation because the relative fO_2 was well buffered by the abundant presence of metallic Fe. For this reason, we have investigated with *in situ* experiments how the stability fields of $Fe_{(1-x)}O$ and $Fe^0 + Fe_3O_4$ in the simple Fe–O system evolve with increasing pressure. At atmospheric pressure and a relative fO_2 of IW, the phase boundary is situated at ~570°C. Only if that temperature increases with increasing pressure (i.e. the size of the stability field of $Fe^0 + Fe_3O_4$ increases) can we assume that disproportionation according to equation (8) indeed takes place. The *in situ* experiments were performed in a MAX80 multi-anvil device at the HASYLAB in Hamburg, from 300 to 550°C and 0·5 to 7·5 GPa. The experimental and analytical techniques are not detailed here but have been described at length by Nover *et al.* (2005) and Mueller *et al.* (2007). Starting materials were mixtures of Fe metal and magnetite powders. The multi-anvil press in Hamburg is coupled to a synchrotron source, so reaction progress (i.e. the reaction of metallic Fe with magnetite to form wüstite) can be monitored *in situ* with white-beam energy-dispersive X-ray diffraction.

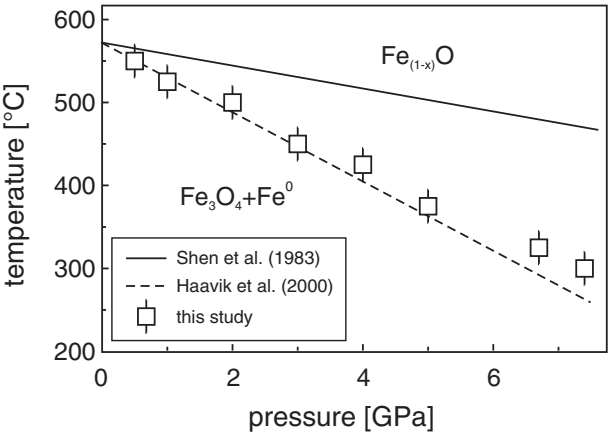

Fig. 12. Magnetite+Fe^0 and wüstite phase boundaries in pressure–temperature space. The continuous line is from quench experiments (Shen *et al.*, 1983), the dashed line is from thermodynamic calculations (Haavik *et al.*, 2000), and the symbols illustrate the position of the phase boundary as determined by *in situ* X-ray diffraction (this study). The univariant equilibrium (i.e. $4FeO = Fe^0 + Fe_3O_4$) has a distinctly negative slope in pressure–temperature space, suggesting that Fe metal + wüstite is the high-temperature assemblage.

Experimental results are shown in Fig. 12. We can confirm that the phase boundary of the disproportionation equilibrium has a distinctly negative slope in pressure–temperature space (i.e. -41 °C GPa^{-1}), implying that the $Fe_{1-x}O$ stability field increases with increasing pressure. This is possible only if the paragenesis Fe metal + wüstite is the high-pressure assemblage. The slope derived here for the univariant equilibrium is considerably steeper than that determined by earlier quench experiments (i.e. -12°C GPa^{-1} by Shen *et al.*, 1983) but coincides closely with the pressure–temperature slope calculated by Haavik *et al.* (2000) with thermodynamic data (Fig. 12). Clearly, with increasing pressure in the simple Fe–O system, wüstite is favored over magnetite + Fe^0 (see also Lazor *et al.*, 2004). If it was only for the simple Fe–O system, there could be no production of ferric iron with increasing pressure solely by FeO disproportionation.

Obviously, however, we have to consider phases other than those stable in the Fe–O system. In systems compositionally more complex than Fe–O, such as a fertile mantle composition, phases can be stabilized that are sinks for ferric iron. When these phases appear, they fractionate any ferric iron present, and a gradient is established around these phases with respect to the chemical potentials of ferric iron components in the phases. The

FeO-bearing components respond to that gradient by breaking down to metallic Fe plus ferric iron, regardless of the phase relations in the simple Fe–O system. In the upper mantle and the Transition Zone, the ferric iron sinks forcing equation (8) to the right are majoritic garnet and subcalcic pyroxene (O'Neill *et al.*, 1993*a*, 1993*b*; Rohrbach *et al.*, 2007), whereas in the lower mantle it is Mg–Si perovskite (McCammon, 1997; Frost *et al.*, 2004). In the Earth's mantle, the most important intensive parameter to stabilize majorite and perovskite is pressure. Therefore, the extent of FeO disproportionation increases with increasing pressure, and relative fO_2 falls with pressure until Fe metal is a stable phase.

Oxidation and reduction under closed-system conditions during mantle convection

When material from the deeper mantle is within the stability field of majoritic garnet and convects upward, majorite becomes unstable. In response, ferric iron components are released. The ferric iron liberated then reacts with metallic Fe to form FeO, until either the metal phase or ferric iron are consumed. The only requirement to achieve oxidation to above Fe metal saturation (i.e. $\Delta\log fO_2$ [IW] > -2 at bulk Mg-number of 0·9) is that majorite breakdown releases per mol metallic Fe at least 2 moles $FeO_{1\cdot5}$ [compare the stoichiometry of equation (8)]. The average metal-free (oxidized) fertile upper mantle composition contains 8·1 wt % total iron of which ~2000 ppm is Fe_2O_3 (O'Neill *et al.*, 1993*a*). In the context of our experiments, we interpret the 2000 ppm Fe_2O_3 as an 'excess' Fe_2O_3 component, left over after all Fe metal was oxidized to FeO. The process described here may be termed 'closed-system oxidation' because it works without the addition of any other oxidizing agent, solely by increasing the activities of the ferric iron components and solely driven by decompression.

In turn, when oxidized upper mantle material is compressed by downward convection to ~8 GPa, the mantle material will experience relative reduction to fO_2 conditions below IW. At around this pressure, corresponding to a depth of ~250 km, majoritic garnet and subcalcic pyroxene have become so abundant and the chemical potentials of the ferric iron components so low that (Fe,Ni) metal becomes a stable phase. Initially, the composition of the metal phase will be Ni-dominated because NiO is reduced to metal more easily than FeO, but as pressure builds up the metal will shift gradually to a more Fe-rich composition.

Ideally, convection leads to an upper mantle that is stratified with respect to fO_2, as observed. The upper 250 km where majoritic garnet is unstable is oxidized because ferric iron liberated from majorite breakdown has eliminated all metallic Fe present. Relative fO_2 in this mantle region is controlled by the activities of the ferrous and ferric iron components in the mantle minerals (compare the FMQ equilibrium). The buffering capacity of that mantle region is low because both ferrous and ferric iron are dilute quantities in the phases. Gradients toward lower relative fO_2 with depth may develop, as demonstrated by Woodland & Koch (2003) for cratonic lithospheric mantle xenoliths in kimberlites. Relative fO_2 in that upper oxidized shell is subject to all mantle processes affecting bulk ferrous/ferric iron ratios and the relative abundances of mantle phases; including partial melting, melt extraction, mantle metasomatism, and cycling of oxidized surface material back into the mantle along convergent plate margins.

Below 250 km, an (Fe,Ni) metal phase is stable. Consequently, the mantle below that depth is well buffered with respect to fO_2. Relative and absolute fO_2 are constrained by the mol fraction of metallic Fe in the (Fe,Ni) alloy and the activities of the ferrous iron components in the coexisting silicates. Once an Fe-dominated metal phase is stable, fO_2 can vary only within very narrow limits, as a shift in fO_2 would require a major shift in the bulk Mg-number of the silicate mantle. The upper limit may be around IW − 0·5 when the metal phase is Ni rich, Ni^0 being produced by reduction of the Ni_2SiO_4 component in olivine. The lower limit will be around IW − 2 where pure Fe metal is in redox equilibrium with a bulk silicate Mg-number of 0·9. So, unless there are systematic variations in bulk mantle composition with depth, relative fO_2 is expected to be narrowly constrained to levels below IW; this constraint applies to about 75 vol. % of the Earth's mantle.

CONCLUSIONS

(1) Electron energy loss spectroscopy (EELS) analyses of high-pressure phases reveal that majoritic garnet and subcalcic pyroxene both fractionate significant amounts of ferric iron, even when they are in redox equilibrium with metallic iron. The amount of ferric iron fractionated by these phases increases with increasing pressure. The source identified for the ferric iron can only be the disproportionation of FeO. *In situ* equilibration experiments in the simple Fe–O system reported here demonstrate that FeO disproportionation occurs only in compositionally complex systems, when phases are stabilized that can fractionate ferric iron. In the upper mantle, the major ferric iron sinks driving FeO into disproportionation are majoritic garnet, followed by subcalcic pyroxene.

(2) We suggest, based on a mass-balance calculation, that a fertile mantle composition may reach Fe metal saturation at around 8 ± 1 GPa. In this pressure interval, sufficient majoritic garnet and pyroxene are stable for the bulk ferric iron of the fertile mantle (~2000 ppm)

to be accommodated in subcalcic pyroxene and majoritic garnet. Ferric iron is incorporated even though these phases are in redox equilibrium with pure metallic Fe. This conclusion is valid only if the composition of the Earth's mantle remains constant with depth, with respect to both FeO and Fe_2O_3, and all other components necessary to stabilize subcalcic clinopyroxene and majoritic garnet. The depth region within which metal saturation is expected to be reached lies around 160 km above the base of the upper mantle, at ~250 km depth.

(3) An upper mantle within (Fe,Ni) metal saturation holds a number of interesting implications. Redox melting may become an attractive and more widely accepted partial melting mode in the mantle (Green *et al.*, 1987; Taylor & Green, 1987; Foley, 1988, 2008, 2010). Carbon–hydrogen–oxygen fluids stable in deeper, metal-saturated mantle are dominated by the reduced species CH_4 and H_2 (Matveev *et al.*, 1997); when these fluids percolate upwards into more oxidized mantle regions, reaction may occur to produce H_2O and CO_2. Both these species will lower the mantle solidus temperature and may trigger partial melting (Dasgupta & Hirschmann, 2006). Beneath mid-ocean ridges (i.e. at 150–300 km depth), diffuse low-velocity zones have been identified where P and S waves are attenuated (Forsyth *et al.*, 1998; Gu *et al.*, 2005) and mantle resistivity is distinctly anisotropic (Evans *et al.*, 1999). Perhaps these low-velocity zones mark the global pressure interval within which metallic (Fe,Ni) solid solutions become unstable; here deep-seated C–H–O fluids are oxidized to H_2O and CO_2, generating thin films along grain boundaries of volatile-rich carbonatitic or hydrous melt that attenuate seismic waves.

(4) In view of the widespread (Fe,Ni) metal saturation, it should also be reconsidered whether the chondritic highly siderophile element signature of the mantle, conventionally attributed to a late chondritic veneer (O'Neill, 1991*a*, 1991*b*) added toward the end of Earth's accretion, is at least in part a 'ghost signature' of a former (Fe,Ni) metal phase (Jones & Drake, 1986), stable at depth but oxidized in the upper mantle.

(5) Given that the modern upper mantle below 250 km is metal-saturated and its relative fO_2 is well buffered around IW − 2, there is no basis to expect that the ancient mantle was any different in terms of fO_2 control. Hence, it should not come as a surprise that no secular variations in the oxidation state of basalts have yet been detected; that is, Archaean mantle melts are as oxidized (or as reduced) as modern mantle melts (Canil, 1997, 2002). Equally unfounded appears to be the expectation that early Archaean volatile emanations from the mantle, via volcanic degassing, were more reduced than volcanic gases of today.

ACKNOWLEDGEMENTS

We thank all colleagues in Münster and Zürich, especially Markus Lagos, Thorsten Geisler-Wierwille and Frank Tomaschek for fruitful discussions. All machine shop members in Münster, especially Paul Löbke and Michael Feldhaus, are thanked for technical assistance. Reviews by Dan Frost and two anonymous reviewers, as well as comments and editorial handling by Jörg Hermann, are greatly appreciated.

FUNDING

This work was supported financially by the German Research Foundation (DFG) grant Ba964/21 to C. Ballhaus and Swiss National Science Foundation (SNFS) grant 2-777-86-06 to M. W. Schmidt.

SUPPLEMENTARY DATA

Supplementary data for this paper are available at *Journal of Petrology* online.

REFERENCES

Akaogi, M. & Akimoto, S. (1979). High-pressure phase equilibria in a garnet lherzolite, with special reference to Mg^{2+}–Fe^{2+} partitioning among constituent minerals. *Physics of the Earth and Planetary Interiors* **19**, 31–51.

Arculus, R. J. (1994). Aspects of magma genesis in arcs. *Lithos* **33**, 189–208.

Ballhaus, C., Berry, R. E. & Green, D. H. (1990). Oxygen fugacity controls in the Earth's upper mantle. *Nature* **348**, 437–440.

Ballhaus, C. G. (1993). Oxidation states of lithospheric and asthenospheric upper mantle. *Contributions to Mineralogy and Petrology* **114**, 331–348.

Ballhaus, C. (1995). Is the upper mantle metal-saturated? *Earth and Planetary Science Letters* **132**, 75–86.

Ballhaus, C. & Frost, B. R. (1994). The generation of oxidized CO_2-bearing basaltic melts from reduced mantle sources. *Geochimica et Cosmochimica Acta* **58**, 4431–4440.

Ballhaus, C. G., Berry, R. F. & Green, D. H. (1991). Experimental calibration of the olivine–orthopyroxene–spinel oxygen barometer—implications for oxygen fugacity in the Earth's upper mantle. *Contributions to Mineralogy and Petrology* **107**, 27–40.

Bell, P. M. & Mao, H. K. (1975). Preliminary evidence of disproportionation of ferrous iron in silicates at high pressures and temperatures. *Carnegie Institution of Washington Yearbook* **74**, 557–559.

Bell, P. M., Mao, H. K., Weeks, R. A. & Valkenburg, A. V. (1976). High-pressure disproportionation study of iron in synthetic basalt glass. *Carnegie Institution of Washington Yearbook* **75**, 515–520.

Bezos, A. & Humler, E. (2005). The $Fe^{3+}/\Sigma Fe$ ratios of MORB glasses and their implications for mantle melting. *Geochimica et Cosmochimica Acta* **69**, 711–725.

Canil, D. (1997). Vanadium partitioning and the oxidation state of Archaean komatiite magmas. *Nature* **389**, 842–845.

Canil, D. (2002). Vanadium in peridotites, mantle redox and tectonic environments: Archean to present. *Earth and Planetary Science Letters* **195**, 75–90.

Canil, D. & O'Neill, H. St. C. (1996). Distribution of Ferric iron in some upper-mantle assemblages. *Journal of Petrology* **37**, 609–635.

Christie, D. M., Carmichael, I. S. E. & Langmuir, C. H. (1986). Oxidation-states of midocean ridge basalt glasses. *Earth and Planetary Science Letters* **79**, 397–411.

Connolly, J. A. D. (1990). Multivariable phase diagrams: an algorithm base on generalized thermodynamics. *American Journal of Science* **290**, 666–718.

Connolly, J. A. D. & Petrini, K. (2002). An automated strategy for calculation of phase diagram sections and retrieval of rock properties as a function of physical conditions. *Journal of Metamorphic Geology* **20**, 697–708.

Dasgupta, R. & Hirschmann, M. M. (2006). Melting in the Earth's deep upper mantle caused by carbon dioxide. *Nature* **440**, 659–662.

Deines, P., Nafziger, R. H., Ulmer, G. C. & Woermann, E. (1976). Temperature–oxygen fugacity tables for selected gas-mixtures in system C–H–O at one atmosphere total pressure. *Metallurgical Transactions B—Process Metallurgy* **7**, 143–143.

Evans, R. L., Tarits, P., Chave, A. D., White, A., Heinson, G., Filloux, J. H., Toh, H., Seama, N., Utada, H., Booker, J. R. & Unsworth, M. J. (1999). Asymmetric electrical structure in the mantle beneath the East Pacific Rise at 17°S. *Science* **286**, 752–756.

Fabrichnaya, O. B. & Sundman, B. (1997). The assessment of thermodynamic parameters in the Fe–O and Fe–Si–O systems. *Geochimica et Cosmochimica Acta* **61**, 4539–4555.

Fei, Y. & Mao, H. K. (1994). *In situ* determination of the NiAs phase of FeO at high pressure and temperature. *Science* **266**, 1678–1680.

Fei, Y., Frost, D. J., Mao, H. K., Prewitt, C. T. & Häusermann, D. (1999). *In situ* determination of the high-pressure phase of Fe_3O_4. *American Mineralogist* **84**, 203–206.

Foley, S. F. (1988). The genesis of continental basic alkaline magmas—an interpretation in terms of redox melting. *Journal of Petrology (Special Lithosphere Issue)* 139–161.

Foley, S. F. (2008). Rejuvenation and erosion of the cratonic lithosphere. *Nature Geoscience* **1**, 503–510.

Foley, S. F. (2010). A reappraisal of redox melting in the Earth's mantle as a function of tectonic setting and time. *J. Petrology* , doi:10.1093/petrology/egq061.

Forsyth, D. W., Scheirer, D. S., Webb, S. C., Dorman, L. M., Orcutt, J. A., Harding, A. J., Blackman, D. K., Morgan, J. P., Detrick, R. S., Shen, Y., Wolfe, C. J., Canales, J. P., Toomey, D. R., Sheehan, A. F., Solomon, S. C., Wilcock, W. S. D. & Team, MS (1998). Imaging the deep seismic structure beneath a mid-ocean ridge: The MELT experiment. *Science* **280**, 1215–1218.

Frost, B. R. & Ballhaus, C. (1998). Comment on 'Constraints on the origin of the oxidation state of mantle overlying subduction zones: An example from Simcoe, Washington, USA'. *Geochimica et Cosmochimica Acta* **62**, 329–331.

Frost, D. J. & Langenhorst, F. (2002). The effect of Al_2O_3 on Fe–Mg partitioning between magnesiowüstite and magnesium silicate perovskite. *Earth and Planetary Science Letters* **199**, 227–241.

Frost, D. J. & McCammon, C. A. (2008). The redox state of the Earth's mantle. *Annual Review of Earth and Planetary Sciences* **36**, 389–420.

Frost, D. J., Liebske, C., Langenhorst, F., McCammon, C. A., Tronnes, R. G. & Rubie, D. C. (2004). Experimental evidence for the existence of iron-rich metal in the Earth's lower mantle. *Nature* **428**, 409–412.

Frost, D. J., Mann, U., Asahara, Y. & Rubie, D. C. (2008). The redox state of the mantle during and just after core formation. *Philosophical Transactions of the Royal Society of London, Series A* **366**, 4315–4337.

Green, D. H., Falloon, T. J. & Taylor, W. R. (1987). Mantle-derived magmas—roles of variable source peridotite and variable C–H–O fluid compositions. In: Mysen, B. O. (ed.) *Magmatic Processes and Physicochemical Principles. Geochemical Society, Special Publications* **1**, 1139–154.

Gu, Y. J., Lerner-Lamb, A. L., Dziewonskic, A. M. & Ekström, G. (2005). Deep structure and seismic anisotropy beneath the East Pacific Rise. *Earth and Planetary Science Letters* **232**, 259–272.

Gudmundsson, G. & Wood, B. J. (1995). Experimental tests of garnet peridotite oxygen barometry. *Contributions to Mineralogy and Petrology* **119**, 56–67.

Haavik, C., Stølen, S., Fjellvåg, H., Hanfland, M. & Häusermann, D. (2000). Equation of state of magnetite and its high-pressure modification: Thermodynamics of the Fe–O system at high pressure. *American Mineralogist* **85**, 514–523.

Herzberg, C. & Zhang, J. Z. (1996). Melting experiments on anhydrous peridotite KLB-1: Compositions of magmas in the upper mantle and transition zone. *Journal of Geophysical Research* **101**, 8271–8295.

Holland, T. J. B. & Powell, R. (1998). An internally consistent thermodynamic data set for phases of petrological interest. *Journal of Metamorphic Geology* **16**, 309–343.

Irifune, T. (1987). An experimental investigation of the pyroxene–garnet transformation in a pyrolite composition and its bearing on the constitution of the mantle. *Physics of the Earth and Planetary Interiors* **45**, 324–336.

Irifune, T. & Isshiki, M. (1998). Iron partitioning in a pyrolite mantle and the nature of the 410-km seismic discontinuity. *Nature* **392**, 702–705.

Jones, J. H. & Drake, M. J. (1986). Geochemical constraints on core formation in the Earth. *Nature* **322**, 221–228.

Kohlstedt, D. L., Keppler, H. & Rubie, D. C. (1996). Solubility of water in the α, β, and γ phases of $(Mg,Fe)_2SiO_4$. *Contributions to Mineralogy and Petrology* **123**, 345–357.

Lauterbach, S., McCammon, C. A., van Aken, P., Langenhorst, F. & Seifert, F. (2000). Mössbauer and ELNES spectroscopy of $(Mg,Fe)(Si,Al)O_3$ perovskite: a highly oxidized component of the lower mantle. *Contributions to Mineralogy and Petrology* **138**, 17–26.

Lazor, P., Shebanova, O. N. & Annersten, H. (2004). High-pressure study of stability of magnetite by thermodynamic analysis and synchrotron X-ray diffraction. *Journal of Geophysical Research* **109(B05201)**, 1–16.

Luhr, J. F. & Carmichael, I. S. E. (1981). The Colima volcanic complex, Mexico: part II. Late Quaternary cinder cones. *Contributions to Mineralogy and Petrology* **76**, 127–147.

Luhr, J. F. & Carmichael, I. S. E. (1985). Jorullo volcano, Michoacfin, Mexico (1759–1774): the earliest stages of fractionation in calcalkaline magmas. *Contributions to Mineralogy and Petrology* **90**, 142–161.

Luth, R. W. & Canil, D. (1993). Ferric iron in mantle-derived pyroxenes and a new oxybarometer for the mantle. *Contributions to Mineralogy and Petrology* **113**, 236–248.

Luth, R. W., Virgo, D., Boyd, F. R. & Wood, B. J. (1990). Ferric iron in mantle-derived garnets. *Contributions to Mineralogy and Petrology* **104**, 56–72.

Mao, H. K. (1974). A discussion of the iron oxides at high pressure with implications for the chemical and thermal evolution of the Earth. *Carnegie Institution of Washington Yearbook* **73**, 510–518.

Mao, H. K. & Bell, P. M. (1977). Disproportionation equilibrium in iron-bearing systems at pressures above 100 kbar with applications to the chemistry of the Earth's mantle. In: Saxena, S. K. &

Bhattacharji, S. (eds) *Energetics of Geological Processes*. New York: Springer, pp. , pp. 236–249.

Matveev, S., Ballhaus, C., Fricke, K., Truckenbrodt, J. & Ziegenbein, D. (1997). C–H–O volatiles under upper mantle conditions. I. Experimental results. *Geochimica et Cosmochimica Acta* **61**, 3081–3088.

McCammon, C. A. (1997). Perovskite as a possible sink for ferric iron in the lower mantle. *Nature* **387**, 694–696.

McCammon, C. & Kopylova, M. G. (2004). A redox profile of the Slave mantle and oxygen fugacity control in the cratonic mantle. *Contributions to Mineralogy and Petrology* **148**, 55–68.

McCammon, C. A. & Ross, N. L. (2003). Crystal chemistry of ferric iron in $(Mg,Fe)(Si,Al)O_3$ majorite with implications for the transition zone. *Physics and Chemistry of Minerals* **30**, 206–216.

McDonough, W. F. & Sun, S. S. (1995). The composition of the Earth. *Chemical Geology* **120**, 223–253.

Mueller, H.-J., Schilling, F. R. & Lathe, C. (2007). Multianvil techniques in conjunction with synchrotron radiation at Deutsches Elektronen SYnchrotron (DESY)–HAmburger SYnchrotron LABor (HASYLAB). In: Ohtani, E. (ed.) *Advances in high-pressure Mineralogy. GSA Special Papers* **421**, 207–226.

Nover, G., Stoll, J. & von der Gönna, J. (2005). Promotion of graphite formation by tectonic stress: a laboratory experiment. *Geophysical Journal International* **160**, 1059–1067.

O'Neill, H. St. C. (1987). The quartz–fayalite–iron and quartz–fayalite–magnetite equilibria and the free energies of formation of fayalite (Fe_2SiO_4) and magnetite (Fe_3O_4). *American Mineralogist* **72**, 67–75.

O'Neill, H. St. C. (1991*a*). The origin of the Moon and the early history of the Earth—A chemical model. Part 1: The Moon. *Geochimica et Cosmochimica Acta* **55**, 1135–1157.

O'Neill, H. St. C. (1991*b*). The origin of the Moon and the early history of the Earth—A chemical model. Part 2: The Earth. *Geochimica et Cosmochimica Acta* **55**, 1159–1172.

O'Neill, H. St. C. & Wall, V. J. (1987). The olivine–orthopyroxene–spinel oxygen geobarometer, the nickel precipitation curve, and the oxygen fugacity of the Earth's upper mantle. *Journal of Petrology* **28**, 1169–1191.

O'Neill, H. St. C., Rubie, D. C., Canil, D., Geiger, C. A., Ross, C. R., Seifert, F. & Woodland, A. B. (1993*a*). Ferric iron in the upper mantle and in Transition Zone assemblages: Implications for relative oxygen fugacities in the mantle. In: Rubie, D. C. (ed.) *Evolution of the Earth and Planets. American Geophysical Union, Geophysical Monograph* **74**, 7473–88.

O'Neill, H. St. C., McCammon, C. A., Canil, D., Rubie, D. C., Ross, C. R. & Seifert, F. (1993*b*). Mössbauer spectroscopy of mantle transition zone phases and determination of minimum Fe^{3+} content. *American Mineralogist* **78**, 456–460.

Palme, H. & O'Neill, H. St. C. (2003). Cosmochemical estimates of mantle composition. In: Carlson, R. W. (ed.) *The Mantle and the Core*, Vol. 2. Oxford: Elsevier–Pergamon, pp. 1–38.

Rohrbach, A., Ballhaus, C., Golla-Schindler, U., Ulmer, P., Kamenetsky, V. S. & Kuzmin, D. V. (2007). Metal saturation in the upper mantle. *Nature* **449**, 456–458.

Saxena, S. K., Chatterjee, N., Fei, Y. & Shen, G. (1993). *Thermodynamic data on oxides and silicates: An assessed data set based on thermochemistry and high pressure phase equilibrium*. Berlin: Springer.

Shen, P., Bassett, W. A. & Liu, L.-G. (1983). Experimental determination of the effects of pressure and temperature on the stoichiometry and phase relations of wüstite. *Geochimica et Cosmochimica Acta* **47**, 773–778.

Sobolev, N. V. & Lavrent'ev, J. G. (1971). Isomorphic sodium admixture in garnets formed at high pressures. *Contributions to Mineralogy and Petrology* **31**, 1–12.

Struzhkin, V. V., Mao, H-k., Hu, J., Schwoerer-Böhning, M., Shu, J., Hemley, R. J., Sturhahn, W., Hu, M. Y., Alp, E. E., Eng, P. & Shen, G. (2001). Nuclear inelastic X-ray scattering of FeO to 48 GPa. *Physical Review Letters* **87**, 255501, 1–4.

Taylor, W. R. & Green, D. H. (1987). The petrogenetic role of methane: Effect on liquidus phase relations and the solubility mechanism of reduced C–H volatiles. In: Mysen, B. O. (ed.) *Magmatic Processes and Physiochemical Principles. Geochemical Society Special Publications* **1**, 1121–138.

van Aken, P. A. & Liebscher, B. (2002). Quantification of ferrous/ferric ratios in minerals: new evaluation schemes of $L_{2,3}$ electron energy-loss near-edge spectra. *Physics and Chemistry of Minerals* **29**, 188–200.

van Aken, P. A., Liebscher, B. & Styrsa, V. J. (1998). Quantitative determination of iron oxidation states in minerals using Fe $L_{2,3}$-edge electron energy-loss near-edge structure spectroscopy. *Physics and Chemistry of Minerals* **25**, 323–327.

Woodland, A. B. & Koch, M. (2003). Variation in oxygen fugacity with depth in the upper mantle beneath the Kaapvaal craton, Southern Africa. *Earth and Planetary Science Letters* **214**, 295–310.

Woodland, A. B. & O'Neill, H. S. C. (1995). Phase relations between $Ca_3Fe_2^{3+}Si_3O_{12}$–$Fe_3^{2+}Fe_2^{3+}Si_3O_{12}$ garnet and $CaFeSi_2O_6$–$Fe_2Si_2O_6$ pyroxene solid solutions. *Contributions to Mineralogy and Petrology* **121**, 87–98.